JOURNAL OF GEOPHYSICAL RESEARCH, VOL. 104, NO. E11, PAGES 27,133–27,142, NOVEMBER 25, 1999

Jupiter's visible aurora and Io footprint

Ashwin R. Vasavada,[1] Antonin H. Bouchez, Andrew P. Ingersoll
Division of Geological and Planetary Sciences, California Institute of Technology, Pasadena

Blane Little and Clifford D. Anger
ITRES Research, Ltd., Calgary, Alberta, Canada

and the Galileo SSI Team

Abstract. Images obtained by the Galileo spacecraft's solid-state imaging (SSI) system represent the first survey of Jupiter's northern auroral emissions at visible wavelengths and on the nightside of the planet. These images captured the emissions with unprecedented spatial resolutions down to ~26 km pixel^{-1}. Four classes of emission were observed: (1) a continuous, primary arc associated with the middle/outer magnetosphere, (2) a variable secondary arc associated with the region just beyond Io's torus, (3) diffuse "polar cap" emission, and (4) a patch and tail associated with the magnetic footprint of Io. The primary arc emission occurs at an altitude 245 ± 30 km above the 1-bar pressure level. Its horizontal width is typically a few hundred kilometers, and its total optical power output varied between ~10^{10} and ~10^{11} W in observations taken months apart. The location of the primary arc in planetary coordinates is similar to that on dayside images at other wavelengths and does not vary with local time. The morphology of the primary arc is not constant, changing from a multiply branched, latitudinally distributed pattern after dusk to a single, narrow arc before dawn. Emission from Io's ionospheric footprint is distinct from both the primary and secondary arcs. Measurements of its optical power output ranged from 2 to 7 × 10^8 W.

1. Background and Introduction

High-energy particles precipitating along magnetic field lines into Jupiter's polar atmosphere deposit energy, some of which is reemitted by a variety of excited gases. Emission has been detected over a wide spectral range, implying a variety of input particle compositions and energies. Earth-orbiting satellites and the Voyager spacecraft first detected ultraviolet (UV) emission from Jupiter's poles in H Lyman and H_2 Lyman and Werner bands [*Herbert et al.*, 1987; *Clarke et al.*, 1980; *Livengood et al.*, 1992]. Precipitation-driven heating of Jupiter's upper atmosphere is detectable in the mid-infrared (IR) [*Kostiuk et al.*, 1977; *Caldwell et al.*, 1980; *Kim et al.*, 1985; *Drossart et al.*, 1986]. Soft X-ray emission may imply that the flux of precipitating particles includes oxygen and sulfur ions in addition to the electrons that most likely cause the UV emission [*Metzger et al.*, 1983; *Waite et al.*, 1994]. Precipitation-created H_3^+ ions emit in the near-infrared (NIR), making the Jovian aurora accessible to ground-based observers [*Drossart et al.*, 1989]. The footprint of Io's flux tube in the Jovian ionosphere was first detected in H_3^+ emission [*Connerney et al.*, 1993]. Recent campaigns using ground-based NIR telescopes and high spatial resolution UV instruments on the Hubble Space Telescope (HST) have resulted in detailed maps of the auroral arcs and the Io footprint on the dayside of the planet [*Clarke et al.*, 1996, 1998; *Prangé et al.*, 1996, 1998; *Kim et al.*, 1994; *Gérard et al.*, 1994; *Grodent et al.*, 1997; *Satoh et al.*, 1996].

Galileo's camera was the first to image the Jovian aurora and Io footprint on the nightside of the planet and to detect auroral emissions at visible wavelengths. Since our initial report [*Ingersoll et al.*, 1998], additional images have been acquired of the north auroral region that greatly extend coverage both in longitude and in local time. Here we discuss the complete data set, placing our results in the context of dayside observations of the aurora at other wavelengths. The primary auroral arc, secondary arcs and patches, diffuse "polar cap" emission, and the Io footprint were detected, depending on the specific geometry and sensitivity of each image. We emphasize the location and morphology of the emissions, revealed by the high spatial resolution of these observations, above their spectral characteristics [*Ingersoll et al.*, 1998]. Auroral emissions can be precisely located in SSI images, revealing their latitude, longitude, and altitude. This information is employed to locate particle source regions in the Jovian magnetosphere through the use of a magnetic field model. The model we employ uses the VIP4 description of the internal field [*Connerney et al.*, 1998] and the magnetodisc model of the external field [*Connerney et al.*, 1981]. Furthermore, Galileo's unique nightside viewpoint resolves ambiguities in the dependence of certain auroral characteristics on local time or longitude.

[1]Now at Department of Earth and Space Sciences, University of California, Los Angeles.

Paper number 1999JE001055.
0148-0227/99/1999JE001055$09.00

2. Observations

Galileo imaged Jupiter's northern aurora between November 1996 and November 1997, during the third, seventh, tenth, and eleventh orbits of the spacecraft's primary mission. Properties of the images used in this study are listed in Table 1. Raw images are available through the Planetary Data System, while images processed for public release have been archived at NASA's Planetary Photojournal.

At visible wavelengths, auroral emissions cannot be distinguished from reflected sunlight. Even on the nightside, the auroral signal appears as fine-scale structure against a diffuse, scattered light background that may be several times brighter. The primary source of scattered light is Jupiter's sunlit crescent. Because the periapses of Galileo's elliptical orbits are on the dayside of Jupiter, the amount of contamination by off-axis scattered light increases with image spatial resolution. Images taken during the third and tenth orbits were taken as the spacecraft was crossing the midnight meridian of Jupiter (solar phase angle of ~180°). They therefore contain the least scattered light and have modest spatial resolutions of 46 and 134 kilometers per pixel (km pix^{-1}) in the image plane, respectively. Images taken during the seventh orbit at a solar phase angle of ~79° contain more scattered light but have a better spatial resolution of 34 km pix^{-1}. The imaging sequence in the eleventh orbit tracked the aurora near 165°W longitude from midnight to dawn (before periapsis), and then from dusk to midnight (after periapsis). These two subsets of images have solar phase angles of ~91° and ~108°, respectively, and have spatial resolutions near 26 km pix^{-1}. Sample images showing the effects of resolution and scattered light are shown in Figure 1. Spacecraft downlink limitations required that nearly all images be summed in 2 × 2-pixel boxes (called HIS mode) before transmission to Earth. The resolutions quoted above are after summation. One image in this study (see Table 1) was returned in full-resolution mode (HIM).

Because the standard Galileo solid-state imaging (SSI) calibration does not account for off-axis light, we manually subtracted the scattered light from the images. The

Table 1. Selected Galileo Primary Mission Images of Jupiter's Aurora

File Name	Date/Time[a]	Orbit[b]	Exposure[c]	Spatial Resolution[d]	Phase Angle, deg	Comment[e]
s0368990100	96-314-06:57:21	C3	51.2 (4)	46.3	179.7	
s0368991100	96-314-07:06:58	C3	1.06 (4)	46.2	179.6	Io
s0389557000	97-092-16:50:59	G7	6.4 (2)	34.2	79.2	Star, H
s0416107845	97-279-03:09:24	C10	8.5 (3)	133.4	179.8	Io
s0416110845	97-279-03:39:44	C10	8.5 (3)	133.5	179.8	Io
s0416112945	97-279-04:00:57	C10	6.4 (3)	133.7	179.7	Io
s0416113600	97-279-04:07:40	C10	12 8 (4)	66.8	179.7	M, Io
s0416113845	97-279-04:10:04	C10	8.5 (3)	133.5	179.7	Io
s0420472100	97-309-18:36:47	E11	6.4 (2)	27.3	92 6	Star
s0420472145	97-309-18:37:17	E11	6.4 (2)	27.3	92.6	Star, H
s0420476700	97-309-19:23:18	E11	6.4 (2)	26.8	91.6	Star
s0420476745	97-309-19:23:48	E11	6.4 (2)	26.8	91.6	Star, H
s0420481400	97-309-20:10:49	E11	6.4 (2)	26.2	90.5	
s0420481445	97-309-20:11:19	E11	6.4 (2)	26.2	90.5	Star, H
s0420486000	97-309-20:57:20	E11	6.4 (2)	25.8	89.3	
s0420486045	97-309-20:57:50	E11	6.4 (2)	25 8	89.3	
s0420815600	97-312-04:29:57	E11	6 4 (2)	25.7	106.5	
s0420815645	97-312-04:30:27	E11	6 4 (2)	25.7	106.5	Io
s0420820100	97-312-05:15:27	E11	6.4 (2)	26.0	107.6	Io
s0420820145	97-312-05:15:57	E11	6.4 (2)	26.0	107.6	
s0420824600	97-312-06:00:57	E11	6.4 (2)	26.5	108.7	Star, Io
s0420824645	97-312-06:01:27	E11	6.4 (2)	26.5	108.7	
s0420829100	97-312-06:46:27	E11	6.4 (2)	27.0	109.7	Star, Io
s0420829145	97-312-06:46:57	E11	6.4 (2)	27.0	109.7	Star, H

[a]The date and universal time of each image are given in the format [year-day of year-hour:minute:seconds].
[b]The letter in the orbit name is the first letter in the name of the primary satellite encountered.
[c]The first number is the exposure time in seconds. The gain state is in parentheses.
[d]The spatial resolution in km pix^{-1} in the image plane at Jupiter's atmosphere.
[e]Star, the pointing was corrected using background stars; H, the image was used to determine emission; M, SSI full-resolution mode (HIM); Io, contains Io footprint emission (also see Table 2).

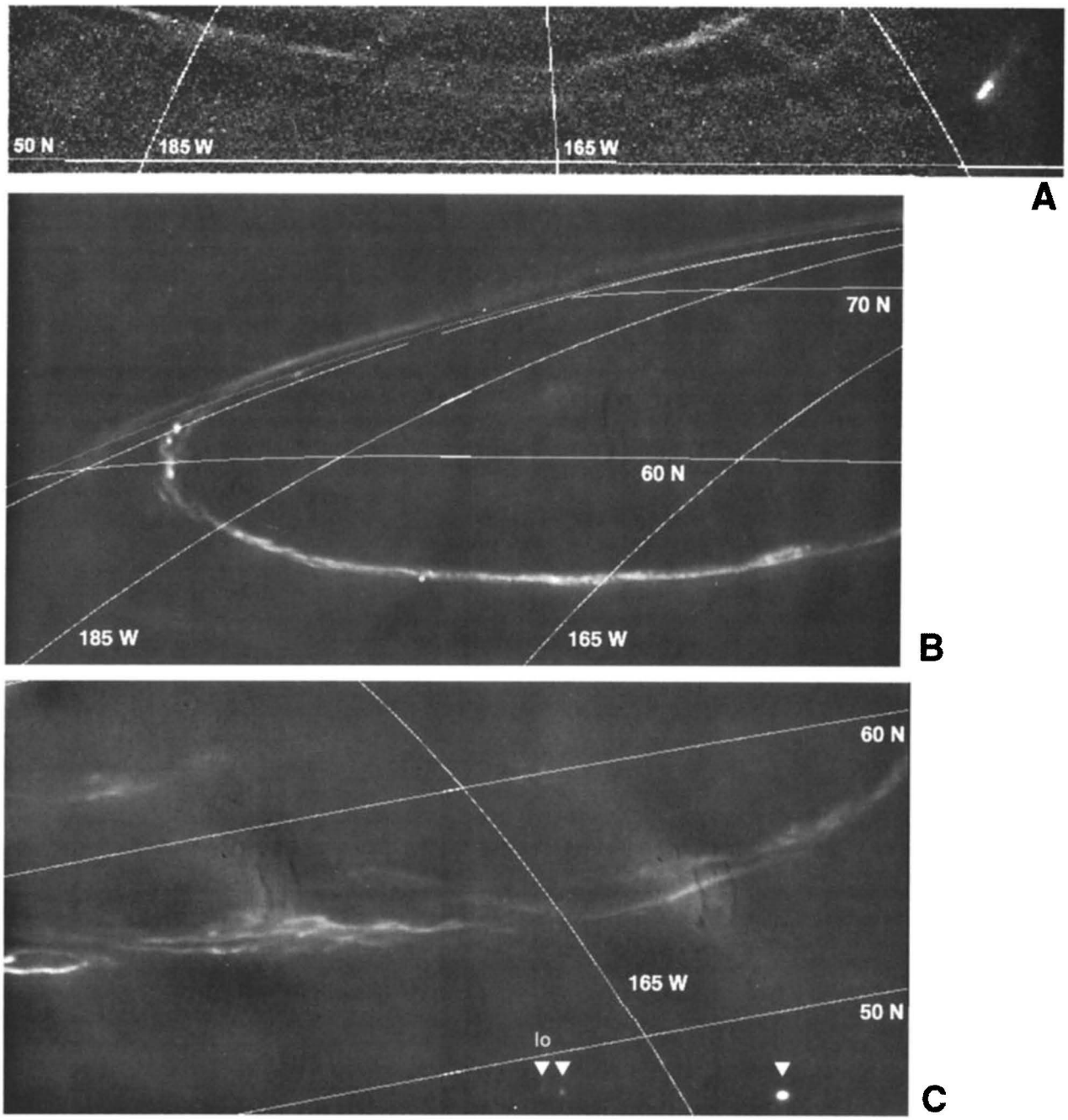

Figure 1. Images of Jupiter's northern auroral region from Galileo's (a) tenth and (b, c) eleventh orbits. Figure 1a (image s0416113600) is centered at local midnight and has a spatial resolution of ~134 km pix^{-1}. It shows emission from the primary arc and a fainter secondary arc, as well as from the Io footprint and tail. The part of the image containing the Io footprint has been reduced in brightness in order to retain detail. Figure 1b (images s0420481400 and s0420481445) is centered at 0300 hours local time and has a spatial resolution of ~26 km pix^{-1}. The finely structured primary arc crosses beyond the planetary limb (plotted at an atmospheric pressure of 1 bar) in the left part of the mosaic. Limb-brightened "polar cap" emission is visible along the limb. Figure 1c (images s0420815600 and s0420815645) shows the same longitudinal segment of the primary arc as Figure 1b at the same spatial resolution. However, the center of Figure 1b is at 2100 hours local time. The features marked with arrows are lightning strikes seen through Jupiter's clouds. The Io footprint is also marked but may not be visible on this reproduction. The images in Figures 1a-1c have been high-pass filtered and adjusted for contrast. However, they have not been remapped or corrected for scattered light. Figure 1c contains diffuse, diagonally aligned scattered light as well as dark, vertically aligned camera blemishes.

background level to be subtracted was determined by sampling the image nearby (but carefully excluding) auroral features. The spectral radiance, I (W m^{-2} sr^{-1} nm^{-1}), of the auroral emission was computed from the background-subtracted data number (DN), the image exposure time and gain state, and the known radiometric response of the detector [*Klaasen et al.*, 1997]. All images in this study were taken with the SSI's clear filter, which has an effective passband of ~385-935 nm (with a tail extending to 1100 nm). The brightness, in Rayleighs ($10^{10}/4\pi$ photons m^{-2} s^{-1} sr^{-1}), of a single pixel was then calculated using both the filter's spectral width and the average energy per photon within its passband. For our images, 1 W m^{-2} sr^{-1} nm^{-1} = 2.12×10^{12} R. In all calculations, the emission was assumed to be isotropic over 4π steradians. The method is similar to that used by *Ingersoll et al.* [1998], but it does not incorporate their geometric factor μ. Apparent auroral brightness increases near the planetary limb, which suggests that the emission is optically thin. Correcting our intensity estimates for this effect would require a detailed geometric model of the emission and is not attempted here.

3. Altitude and Width of the Primary Arc

We were able to determine the altitude of the primary arc emission by observing it on the planetary limb (e.g., Figure 1b) in five high-resolution images that contain identifiable background stars (see Table 1). The image navigation program, NAV, from the Video Image Communication and Retrieval (VICAR) image processing library (distributed by the Multimission Image Processing Lab of the Jet Propulsion Laboratory) uses background stars to derive the pointing of the SSI to an accuracy of ±1 pixel. We used a version of NAV modified by Brian Carcich of Cornell University to interface with the Hubble Space Telescope Guide Star Catalog. Voyager radio occultations have determined that the 1-bar pressure level in Jupiter's atmosphere is coincident with an oblate spheroid with equatorial and polar radii of 71,492 and 66,854 km, respectively [*Lindal et al.*, 1981]. On each image we used NAV to plot several limbs calculated from oblate spheroids with equatorial and polar radii of lengths H greater than those that define the 1-bar level. We then found the value of H that produced the best match (by eye) between the plotted limb and the brightness centroid of the arc (at the point where it crosses the limb).

Using the results from all five images, we found H to be 245 ± 30 km. Galileo probe measurements near Jupiter's equator determined that this altitude range corresponds to a pressure range of roughly 6 to 70 μbar [*Seiff et al.*, 1998]. The emission has a vertical full width at half maximum (FWHM) of 120 ± 30 km and drops below the detection limit at a full width (FW) of 350 ± 70 km. The arc remains detectable from beyond the limb until it drops below a tangential height of 120 ± 40 km, near the altitude of an observed stratospheric haze layer [*Rages et al.*, 1999]. Diffuse "polar cap" emission, also at height H, is detectable when viewed on the limb. Hereafter we assume that all observed emission occurs at altitude H in order to define a reference ellipsoid upon which to measure planetocentric latitudes and System III west longitudes inward from the limb.

The measured altitude of the visible emission is somewhat lower than that of the UV emission, consistent with the simple idea that it results from more energetic particles that penetrate deeper into the atmosphere. Pressure levels derived from UV spectral fits range from <1 μbar to tens of microbars [*Trafton et al.*, 1994; *Clarke et al.*, 1994; *Kim et al.*, 1997; *Ajello et al.*, 1998]. Direct height measurements of the primary arc on UV images range from 300 to 700 km [*Clarke et al.*, 1996; *Grodent et al.*, 1997; *Prangé et al.*, 1998]. Our height value is closer to the derived height of IR enhancements [*Drossart et al.*, 1993]. All are consistent with primary particle energies of tens to hundreds of keV [*Ajello et al.*, 1998].

Figure 2 shows a profile across the primary arc near 166°W as viewed on Jupiter's disc. This profile was created with two images chosen for their large combined dynamic range of 10^4. The central emission from the arc is sharply peaked, with a horizontal width of ~400 km (FWHM). However, an extended skirt is detectable to >3500 km (FW). Both the extreme width of the skirt and its asymmetry in latitude may be the result of scattering and reflections from lower cloud decks. The FWHM measured on other images ranged from 170 to 460 km. We believe that this range reflects differences in viewing geometry and signal-to-noise ratios, as well as temporal and/or spatial brightness variations of the emission. By comparison, widths measured on UV images have been as small as 80 km but generally are several hundred kilometers [*Prangé et al.*, 1998].

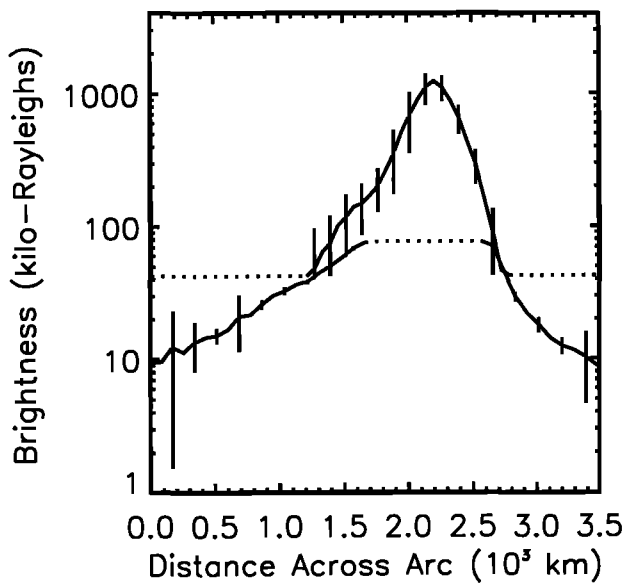

Figure 2. Brightness profiles across the primary arc near 166°W. The profiles run from south to north, with distance measured along Jupiter's spheroid. The figure shows two profiles, each composed of solid and dotted segments. These profiles come from two images, taken about 1 year apart, with different exposure settings resulting in a combined dynamic range of ~10^4. The local times are ~0400 and ~2300 hours, respectively, and avoid the branched configuration of the arc. Image s0420481400 (upper line) resolves the bright core of the emission (solid), but not the faint skirt (dotted). Image s0368990100 (lower line) resolves the skirt (solid) but is saturated in the core (dotted). Each line is actually the average of many profiles created from adjacent columns in the image. The error bars show the variance among these columns.

4. Location of Auroral Features

Plate 1 shows the locations in planetary coordinates of the visible primary auroral arc, secondary arcs, and the Io footprints. The top panel displays measurements made on images taken in the tenth orbit. Because none of these images contains background stars, we could not determine the offset between the commanded and actual pointing of the camera. Previous experience fitting dayside SSI images to Jupiter's limb suggests that the uncorrected camera pointing error in both the line and sample directions is ±5 HIS pixels [*Vasavada et al.*, 1998]. An upper limit to the error in determining the position of a pixel on the ellipsoid (in kilometers along the planet's surface) is the pointing error multiplied by the spatial resolution and divided by the cosine of the emission angle of the pixel. For an emission angle of 60° the error is ±1340 km (±1.1° in planetary coordinates) and ±250 km (±0.2°) for spatial resolutions of 134 and 25 km pix^{-1}, respectively. The bottom panel of Plate 1 displays measurements made on eight eleventh-orbit images that contained identifiable background stars (see Table 1). The pointing error for these images is ±1 pixel.

The measured location of the aurora can be compared with contours generated by a magnetic field model [*Connerney et al.*, 1981; 1998]. Each contour is labeled according to the distance from the planet where contour-crossing field lines intersect the magnetic equator. If the particles that cause the primary arc emission come from a radially symmetric, equatorial region in the magnetosphere, and the model correctly maps this region onto Jupiter, then the observed arc would be parallel to the model contours. In fact, we find that the primary arc parallels the model contours over only a narrow range of longitudes. It follows the 13 R_J contour from 155°W to 175°W. Westward of 175°W, the arc appears at lower R_J contours (crossing south of 9.5 R_J), while eastward of 155°W it turns sharply poleward (crossing the 30 R_J contour). The location of the primary arc is nearly identical in images from the third, seventh, tenth, and eleventh orbits [cf. *Ingersoll et al.*, 1998, Figure 4]. This is true despite the large range of local times in these observations, and the large departures of the primary arc from constant model contours.

A faint secondary arc was distinguished from scattered light in images from the tenth and eleventh orbits, as shown in Figure 1. The tenth-orbit images contain a nearly continuous secondary arc that intersects the 8 R_J model contour at 205°W, the 10 R_J contour at 185°W, and the 8.5 R_J contour at 145°W. Three images from the eleventh orbit exhibit an apparently patchy secondary arc that lies at 7 R_J at 205°W, between 8 and 8.5 R_J from 185°W to 165°W, and at 6 R_J at 150°W. In every case the secondary arc is clearly separate from both the primary arc and the Io footprint (when present). Although the location of the primary arc is the same in both the tenth and eleventh orbits, the secondary arc is consistently at lower R_J contours in the eleventh orbit. Yet in both cases the primary and secondary arcs are roughly parallel west of 160°W and gradually diverge east of that longitude.

5. Morphology and Behavior

The eleventh-orbit time series of the aurora has relatively low sensitivity and high spatial resolution. As a result, it resolves only the brightest emissions, but it captures their structure in rich detail. The primary arc appears segmented, wavy, braided, or branched at different locations and times. The secondary arc is more diffuse and has less apparent structure.

Figure 3 shows six time steps of the primary arc between 150°W and 190°W. In each time step the arc has been unwrapped from the planet along a best fit ellipse. Images of the scattered light background were created by densely sampling nonaurora pixels and interpolating bilinearly between them. These background light images were then subtracted from the raw images. This procedure preserved only the emission from regions both less than ~2000 km in their smallest dimension and more than ~2 DN above background.

By scanning Figure 3 from top to bottom, one can follow the evolution of the arc throughout the night from just after sunset to just before sunrise. The primary arc is visible throughout the range of local times. The presence of a coherent arc (or multiple arcs) east of 160°W contrasts with the transition to diffuse emission noted in most UV studies. Also evident is the change in morphology from a wide, multiply branched arc at dusk to a single, thin arc at dawn. For example, near 175°W the total width of the arc is over 2000 km at 1930 hours local time but is only a few hundred kilometers at 0500 hours (using a 24-hour convention). We have not found any morphological features that vary with local time, with magnetic local time (the local time in the magnetosphere where the associated field lines cross the magnetic equator), or with the orbital positions of any moon. However, it can perhaps be argued that certain features either remain fixed in longitude, or drift westward ~4°-5° in the 45 min between successive observations.

6. Brightness and Power

The aurora at visible wavelengths is probably dominated by emission from molecular hydrogen and the Balmer series lines of atomic hydrogen [*Ingersoll et al.*, 1998; *James et al.*, 1998]. The brightness of the emission varies, due to both real variations and changes in the viewing geometry. The measurements quoted below are approximate.

The primary arc contains segments separated by hundreds of kilometers that are up to several times brighter than the regions that connect them. In the eleventh orbit these segments had a typical brightness of ~1.3 MR, though they increased in brightness when viewed foreshortened along the line of sight. The brightest eleventh-orbit emission was ~6.6 MR, observed when the primary arc was viewed tangent to the line of sight crossing the planetary limb. The secondary arc was typically ~50 kR, though it increased to ~270 kR when viewed near the limb. Diffuse "polar cap" emission was detected when latitudes poleward of the secondary arc were viewed on the limb (e.g., Figure 1b). It reached a maximum brightness of ~390 kR near the magnetic pole.

The brightness estimates given above were computed from single pixels that were chosen subjectively. However, there are significant pixel-to-pixel brightness variations. The power per unit length probably provides a more representative estimate of the brightness, since its measurement incorporates many pixels. We computed this quantity by summing the total power emitted from a short

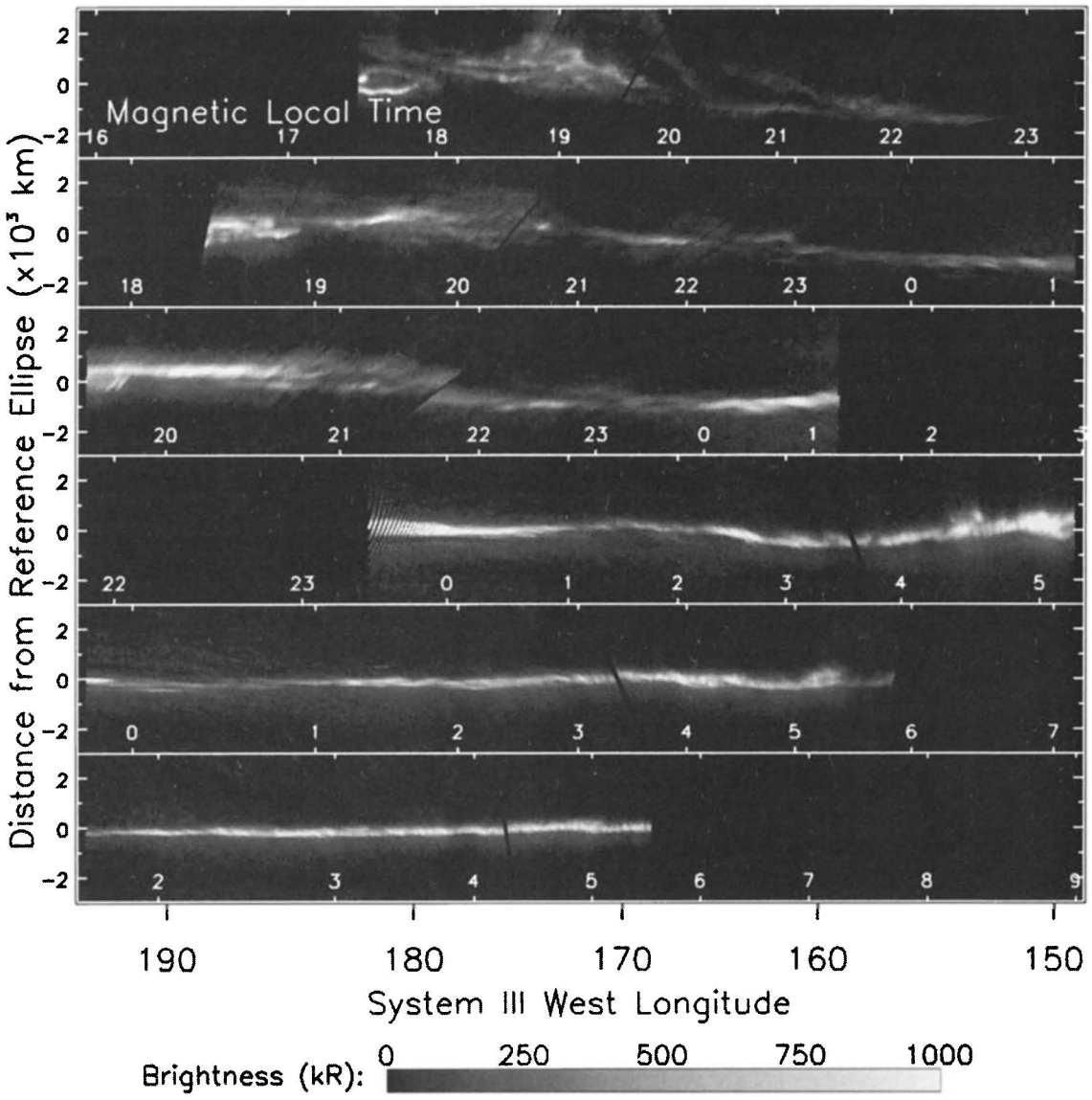

Figure 3. A time series of the northern primary arc through the Jovian night. The six 1×2 image mosaics from Galileo's eleventh orbit increase in local time from (top) dusk to (bottom) dawn. Although the sequence is continuous in local time, there is a 55.5-hour gap between the bottom three panels (images s0420476700-86045 taken before periapsis) and the top three panels (images s0420815600-24645 taken after periapsis). The panels have been aligned in System III longitude and are marked with magnetic local time. The arc is fractured and latitudinally extended in the late evening and narrows through the night. Each pixel of data has been remapped according to its distance from a reference ellipse which was empirically fit to the primary arc. The extremes of each strip may be affected by limb brightening.

(~1°) segment along the arc and then dividing by that length, similar to the method of *Ingersoll et al.* [1998].

We measured values of 350, 80, and 80 W m^{-1} on premidnight segments of the primary arc near 160°W on images from the third, seventh, and tenth orbits, respectively. Measurements from the eleventh orbit yielded values from 150 to 860 W m^{-1}. This wide range of values is partly attributable to the fine structure revealed by the high spatial resolution of the eleventh-orbit images. In general, the power output of the primary arc was several times greater in the third and eleventh orbits than it was in the seventh and tenth orbits. If we assume that the above values are typical of the entire length of the auroral oval, they suggest that the total power output at visible wavelengths is ~10^{10} - 10^{11} W.

7. Io's Footprint

Io's motion relative to Jupiter's magnetosphere induces a ~400 kV potential drop across Io's interior and/or ionosphere. This, in turn, drives a ~3×10^{6} A current of ions which precipitate along Io-crossing field lines into Jupiter's ionosphere, causing auroral emission. Emission at the northern ionospheric footprint of Io-crossing field lines was

unambiguously detected in 10 images from the third [*Ingersoll et al.*, 1998], tenth, and eleventh orbits (see Tables 1 and 2). As shown in Plate 1, the observed footprint appears close to the 5.9-R_J model contour between ~170 and 200°W. The footprints deviate southward of constant model contours between ~135 and 170°W, much like the secondary arc. Additional observations are needed to determine if the southward deviation is a longitude or local time effect. However, because Io is located deep within Jupiter's magnetosphere, a local time dependence is unlikely.

If the Io-Jupiter circuit is closed in Jupiter's ionosphere (the "DC Circuit Model"), then the emission should lead the magnetic field model footprint location by up to 12° longitude [*Goldreich and Lynden-Bell*, 1969]. If, instead, the circuit is closed at the fronts of Alfvén waves radiated from Io, then the lead angle of the emission should vary according to the plasma density along the path between Io and Jupiter [*Drell et al.*, 1965; *Goertz*, 1980; *Neubauer*, 1980; *Bagenal*, 1983]. In this study the footprints have small lead angles of 0°-2° longitude, similar to what is measured in the UV data [e.g., *Prangé et al.*, 1998]. These data are more consistent with the Alfvén wave model, which predicts near-zero lead angles in the longitude range present in our data but larger lead angles elsewhere. However, greater longitude coverage is needed to confidently establish a trend. Furthermore, the longitudes of the Io footprint predicted by the magnetic field model are uncertain by at least a few degrees [*Connerney et al.*, 1998].

In the third and tenth orbits the footprint appears as a roughly circular patch with a diameter of 450 ± 100 km (FWHM), similar to the FWHM of the UV footprint [*Prangé et al.*, 1998]. This diameter suggests either a source region larger than Io's solid body [*Goldreich and Lynden-Bell*, 1969], or drifting and/or scattering (in pitch angle) of precipitating particles. Emission also occurs in a tail which extends eastward along Io's magnetic latitude (Figure 1a). The brightest pixels emit ~0.2-1 MR, while the footprints have total power outputs of ~2-7 × 10^8 W. This range of values is partly attributable to the low signal-to-noise levels and the difficulty of background subtraction.

Images from the eleventh orbit resolve only the brightest emission and therefore were not used to estimate the total power output. Each eleventh-orbit footprint appears as a pair of patches separated by ~0.5° longitude. The eastern component might be the beginning of a tail, although these images lack the obvious extended tails described above. However, these footprints do have short, very faint tails which extend along lines of magnetic longitude toward the magnetic pole. These tails are seen when Jupiter's dipole is tilted toward Io. In this orientation, Io is at its highest Jovicentric latitude and is temporarily outside of its plasma torus. The unusual structure of this emission suggests a more complex model of the interaction between Io and Jupiter than the models described above [*Crary and Bagenal*, 1997].

Some SSI images may have included the positions of the magnetic footprints of Europa and Ganymede. However, corresponding auroral emissions could not be unambiguously detected or confidently ruled out.

8. Implications for Auroral Processes

By observing the aurora on Jupiter's nightside, Galileo has helped to resolve the local time/longitude ambiguity which affects Earth-based observations. Specifically, primary arc emission is observable at all local times, and its location is not time-dependent. As shown in Plate 1, the nightside primary arc closely parallels the dayside reference oval derived from HST Wide Field and Planetary Camera 2 (WFPC2) images [*Clarke et al.*, 1998] between longitudes 155°W and 210°W, even where they both diverge from model magnetic field contours. The visible arc appears to be located at slightly lower (~1°) latitudes between 150°W and 190°W. The HST Faint Object Camera, WFPC2, and ground-based H3+ images show similar primary arc locations [*Prangé et al.*, 1998; *Gérard et al.*, 1994; *Grodent et al.*, 1997; *Satoh et al.*, 1996]. The poleward deflection of the primary arc at longitudes <155°W is seen in some HST images. It may be the "transpolar emission" noted in some studies [*Gérard et al.*, 1994; *Prangé et al.*, 1998] or the

Table 2. Observations of Io's Footprint Emission

File Name	Spacecraft Position[a], deg	Io Orbital Position[a], deg	Footprint Latitude, deg	Footprint Longitude, deg	Io Phase[b], deg
s0368991100	157	80	62.0	125	78
s0416107845	133	82	63.7	126	51
s0416110845	151	96	58.3	134	55
s0416112945	164	105	53.9	140	59
s0416113600	168	109	53.6	142	59
s0416113845	169	110	53.4	142	60
s0420815645	180	172	48.6	168	295
s0420820100	206	193	50.8	179	301
s0420824600	233	214	53.8	191	307
s0420829100	259	235	59.2	204	314

[a]Given as sub-Jovian System III west longitude.
[b]The angle between the Sun, Jupiter, and Io. Phase angles of 0° and 90° occur when Io is above the midnight and dawn meridians, respectively.

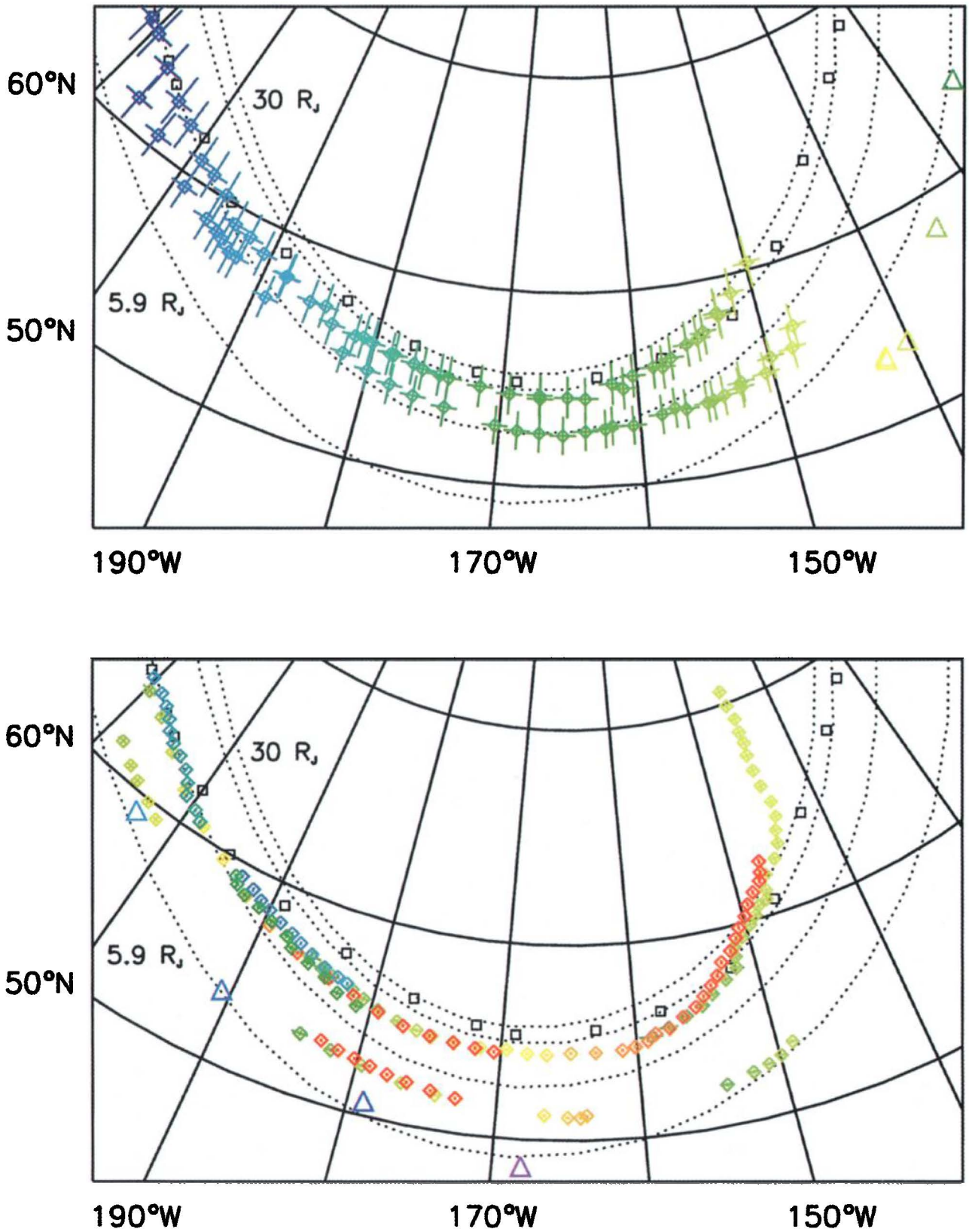

Plate 1. The locations of auroral features during Galileo's (top) tenth and (bottom) eleventh orbits. The observed locations of the primary and secondary arcs (diamonds with error bars) and the Io footprint emission (triangles) were sampled from our images and are displayed on a polar orthographic map. Stars were present in images from the eleventh orbit, resulting in small position uncertainties. The local time at the point of emission is indicated using a color spectrum; violet, green, and red represent 1900, 0, and 0400 hours, respectively. Model magnetic field lines [*Connerney et al.*, 1981, 1998] that cross the magnetic equator at 5.9, 9.5, 15, and 30 R_J intersect our reference ellipsoid at the locations of the dotted lines. The location of the UV primary arc in HST WFPC2 images [*Clarke et al.*, 1998] is marked by squares (without error bars).

poleward state of the "equatorward surge" in others [*Clarke et al.*, 1998].

The morphology and total width of the primary arc do vary with local time. Several HST studies have suggested that the primary arc varies from a narrow state at dawn into diffuse, latitudinally extended emission at dusk. Galileo has observed a similar variation in reverse on the night side (Figure 3). However, SSI observations of the dawn terminator have not captured any of the "dawn storms" noted in HST images.

Any attempt to use imaging data to infer the source regions of precipitating particles suffers from uncertainties in image navigation, the assigned altitude of the emissions, and the adopted model of the magnetic field. Historically, different investigators have associated auroral emissions with regions in Jupiter's magnetosphere at distances varying from 6 to >30 R_J, and therefore with various mechanisms: the Io torus, the corotation boundary, or the boundary between "open" and "closed" field lines. More recently, both the detection of Io's footprint emission and better image spatial resolution have led to the realization that the primary arc is associated with a source region farther out than 6 R_J. Since the secondary arc in the SSI images is distinct from both Io's footprint and the primary arc, its source particles must come from an intermediate region.

A comparison of the visible, UV, and NIR primary arcs reveals that they share several characteristics, most notably their location. The past association of these emissions with field lines ≥30 R_J was biased by poorly fit observations of the southern aurora. When one considers the northern arc alone, most HST data suggest a source region between 9 and 30 R_J (using the same magnetic field model as this study) and therefore a mechanism related either to the magnetodisc or to the corotation boundary.

Energetic heavy ions were originally proposed to explain the UV primary arc [*Herbert et al.*, 1987]. Based on in situ Voyager data, this scheme involved heavy ions diffusing outward from the Io torus and being accelerated. Some of these ions then diffuse inward and are pitch-angle scattered toward Jupiter [*Gehrels and Stone*, 1983]. While no longer applicable to the primary arc, this process offers an explanation of the X-ray aurora, and its associated source region is consistent with the location of the visible secondary arc. Precipitation from this region may also result in the NIR "polar collar" [*Satoh et al.*, 1996] and the UV "low latitude belt" [*Prangé et al.*, 1998].

Considering these inferences, together with the need for both electron and ion populations to explain the spectral variety of emissions, there appears to be evidence for at least three distinct auroral processes: (1) visible, UV, and NIR primary arc emission, all driven by electrons from the middle or outer magnetosphere; (2) visible secondary arc and X-ray emission, both driven by energetic heavy ions from the inner magnetosphere, and (3) Io footprint emission driven by electrons from ~5.9 R_J. There is evidence for additional processes not included above, such as the precipitation that causes low-latitude NIR and UV emissions [*Satoh et al.*, 1996; *Prangé et al.*, 1998], secondary arcs poleward of the primary arc [*Prangé et al.*, 1998], and the "polar cap" emission.

New insights will continue to come both from Galileo and Cassini in situ observations of Jupiter's magnetosphere and through improvements in models of the magnetosphere and its dynamics.

Acknowledgments. We wish to thank two anonymous reviewers, Claudia Alexander, Scott Bolton, John Clarke, Jack Connerney, Renée Prangé, Wayne Pryor, Kent Tobiska, and Hunter Waite for exchanging data and ideas. We also thank Herb Breneman, Todd Jones, Dave Senske, and the JPL Multimission Image Processing Lab for the planning and delivery of the Galileo images. Finally, we thank Lisa Crowell for providing us with satellite ephemeris data. This work was supported by the Galileo Project, NASA, and NSERC of Canada (B.L.).

References

Ajello, J., et al., Galileo orbiter ultraviolet observations of Jupiter aurora, *J. Geophys. Res.*, *103*, 20,125-20,148, 1998.

Bagenal, F., Alfvén wave propagation in the Io plasma torus, *J. Geophys. Res.*, *88*, 3013-3025, 1983.

Caldwell, J., A. T. Tokunaga, and F. C. Gillett, Possible infrared aurorae on Jupiter, *Icarus*, *44*, 667-675, 1980.

Clarke, J. T., H. W. Moos, S. K. Atreya, and A. L. Lane, Observations from Earth orbit and variability of the polar aurora on Jupiter, *Astrophys. J.*, *241*, L179-L182, 1980.

Clarke, J. T., L. B. Jaffel, A. Vidal-Madjar, G. R. Gladstone, J. H. Waite Jr., R. Prangé, J. C. Gérard, J. Ajello, and G. James, Hubble Space Telescope Goddard High-Resolution Spectrograph H_2 rotational spectra of Jupiter's aurora, *Astrophys. J.*, *430*, L73-76, 1994.

Clarke, J. T., et al., Far-ultraviolet imaging of Jupiter's aurora and the Io "Footprint", *Science*, *274*, 404-409, 1996.

Clarke, J. T., et al., Hubble Space Telescope imaging of Jupiter's UV aurora during the Galileo orbiter mission, *J. Geophys. Res.*, *103*, 20,217-20,236, 1998.

Connerney, J. E. P., M. H. Acuña, and N. F. Ness, Modeling the jovian current sheet and inner mangnetosphere, *J. Geophys. Res.*, *86*, 8370-8384, 1981.

Connerney, J. E. P., R. Baron, T. Satoh, and T. Owen, Images of excited H_3^+ at the foot of the Io flux tube in Jupiter's atmosphere, *Science*, *262*, 1035-1038, 1993.

Connerney, J. E. P., M. H. Acuña, N. F. Ness, and T. Satoh, New models of Jupiter's magnetic field constrained by the Io flux tube footprint, *J. Geophys. Res.*, *103*, 11,929-11,939, 1998.

Crary, F. J., and F. Bagenal, Coupling the plasma interaction at Io to Jupiter, *Geophys. Res. Lett.*, *24*, 2135-2138, 1997.

Drell, S. D., H. M. Foley, and M. A. Ruderman, Drag and propulsion of large satellites in the ionosphere: An Alfvén propulsion engine in space, *J. Geophys. Res.*, *70*, 3131-3146, 1965.

Drossart, P., B. Bézard, S. Atreya, J. Lacy, E. Serabyn, A. Tokunaga, and T. Encrenaz, Enhanced acetylene emission near the north pole of Jupiter, *Icarus*, *66*, 610-618, 1986.

Drossart, P., et al., Detection of H_3^+ on Jupiter, *Nature*, *340*, 539-541, 1989.

Drossart, P., B. Bézard, S. K. Atreya, J. Bishop, J. H. Waite Jr., and D. Boice, Thermal profiles in the auroral regions of Jupiter, *J. Geophys. Res.*, *98*, 18,803-18,811, 1993.

Gehrels, N., and E. C. Stone, Energetic oxygen and sulfur ions in the jovian magnetosphere and their contribution to the auroral excitation, *J. Geophys. Res.*, *88*, 5537-5550, 1983.

Gérard, J.-C., V. Dols, R. Prangé, and F. Paresce, The morphology of the north jovian ultraviolet aurora observed with the Hubble Space Telescope, *Planet. Space Sci.*, *42*, 905-917, 1994.

Goertz, C. K., Io's interaction with the plasma torus, *J. Geophys. Res.*, *85*, 2949-2956, 1980.

Goldreich, P., and D. Lynden-Bell, Io, a jovian unipolar inductor, *Astrophys. J.*, *156*, 59-78, 1969.

Grodent, D., G. R. Gladstone, J. C. Gérard, V. Dols, and J. H. Waite, Simulation of the morphology of the jovian UV north aurora observed with the Hubble Space Telescope, *Icarus*, *128*, 306-321, 1997.

Herbert, F., B. R. Sandel, and A. L. Broadfoot, Observations of the jovian UV aurora by Voyager, *J. Geophys. Res.*, *92*, 3141-3154, 1987.

Ingersoll, A. P., A. R. Vasavada, B. Little, C. D. Anger, S. J. Bolton, C. Alexander, K. P. Klaasen, W. K. Tobiska, and the

Galileo SSI Team, Imaging Jupiter's aurora at visible wavelengths, *Icarus*, *135*, 251-264, 1998.

James, G. K., J. M. Ajello, and W. R. Pryor, The middle ultraviolet-visible spectrum of H_2 excited by electron impact, *J. Geophys. Res.*, *103*, 20,113-20,123, 1998.

Kim, S. J., J. Caldwell, A. R. Rivolo, R. Wagener, and G. S. Orton, Infrared polar brightening on Jupiter, III., Spectrometry from the Voyager 1 IRIS experiment, *Icarus*, *64*, 233-248, 1985.

Kim, Y. H., S. J. Kim, J. A. Stuewe, J. Caldwell, and T. M. Herbst, Jovian auroral ovals inferred from infrared H3+ images, *Icarus*, *112*, 326-336, 1994.

Kim, Y. H., J. L. Fox, and J. J. Caldwell, Temperature and altitude of jovian ultraviolet aurora inferred from GHRS observations with the Hubble Space Telescope, *Icarus*, *128*, 189-201, 1997.

Klaasen, K. P., M. J. S. Belton, H. H. Breneman, A. S. McEwen, M. E. Davies, R. J. Sullivan, C. R. Chapman, G. Neukum, and C. M. Heffernan, Inflight performance characteristics, calibration, and utilization of the Galileo solid-state imaging camera, *Opt. Eng.*, *36*, 3001-3027, 1997.

Kostiuk T., M. J. Mumma, J. J. Hillman, D. Buhl, L. W. Brown, J. L. Faris, and D. L. Spears, NH_3 spectral line measurements on Earth and Jupiter using a 10 μm superheterodyne receiver, *Infrared Phys.*, *17*, 431-439, 1977.

Lindal, G. F., et al., The atmosphere of Jupiter: An analysis of the Voyager radio occultation measurements, *J. Geophys. Res.*, *86*, 8721-8727, 1981.

Livengood, T. A., H. W. Moos, G. E. Ballester, and R. M. Prangé, Jovian ultraviolet auroral activity, 1981-1991, *Icarus*, *97*, 26-45, 1992.

Metzger, A. E., D. A. Gilman, J. L. Luthey, K. C. Hurley, H. W. Schnopper, F. D. Seward, and J. D. Sullivan, The detection of X rays from Jupiter, *J. Geophys. Res.*, *88*, 7731-7741, 1983.

Neubauer, F. M., Nonlinear standing Alfvén wave current system at Io: Theory, *J. Geophys. Res.*, *85*, 1171-1178, 1980.

Prangé, R., D. Rego, D. Southwood, P. Zarka, S. Miller, and W. Ip, Rapid energy dissipation and variability of the Io-Jupiter electrodynamic circuit, *Nature*, *379*, 323-325, 1996.

Prangé, R., D. Rego, L. Pallier, J. E. P. Connerney, P. Zarka, and J. Queinnec, Detailed study of FUV jovian auroral features with the post-COSTAR HST faint object camera, *J. Geophys. Res.*, *103*, 20,195-20,215, 1998.

Rages, K., R. Beebe, and D. Senske, Jovian stratospheric hazes: The high phase angle view from Galileo, *Icarus*, *139*, 211-226, 1999.

Satoh, T., J. E. P. Connerney, and R. L. Baron, Emission source model of Jupiter's H_3^+ aurorae: A generalized inverse analysis of images, *Icarus*, *122*, 1-23, 1996.

Seiff, A., D. B. Kirk, T. C. D. Knight, R. E. Young, J. D. Mihalov, L. A. Young, F. S. Milos, G. Shubert, R. C. Blanchard, and D. Atkinson, Thermal structure of Jupiter's atmosphere near the edge of a 5-micron hot spot in the North Equatorial Belt, *J. Geophys. Res.*, *103*, 22,857-22,890, 1998.

Trafton, L. M., J. C. Gérard, G. Munhoven, and J. H. Waite Jr., High-resolution spectra of Jupiter's northern auroral ultraviolet emission with the Hubble Space Telescope, *Astrophys. J.*, *421*, 816-827, 1994.

Vasavada, A. R., et al., Galileo imaging of Jupiter's atmosphere: The Great Red Spot, equatorial region, and White Ovals, *Icarus*, *135*, 265-275, 1998.

Waite, J. H., Jr., F. Bagenal, F. Seward, C. Na, G. R. Gladstone, T. E. Cravens, K. C. Hurley, J. T. Clarke, R. Elsner, and S. A. Stern, ROSAT observations of the Jupiter aurora, *J. Geophys. Res.*, *99*, 14,799-14,809, 1994.

C. D. Anger and B. Little, ITRES Research, Ltd., 2635 37th Avenue NE, Calgary, AL T1Y 5Z6, Canada.

A. H. Bouchez and A. P. Ingersoll, Division of Geological and Planetary Sciences, California Institute of Technology, Pasadena, CA 91125.

A. R. Vasavada, Department of Earth and Space Sciences, University of California, Los Angeles, CA 90095-1567. (ash@mvacs.ess.ucla.edu).

(Received April 1, 1999; revised July 12, 1999;
accepted July 13, 1999)